


# Slotted Fibonacci Spiral Metasurfaces for Microwaves Polarization Control

William O. F. Carvalho 

**Abstract**—This paper presents a metasurface comprised by slotted Fibonacci spiral-like unit-cells built on a copper laminate over a substrate, capable to control the reflection and transmission of linearly polarized (LP) microwaves. The spiral pattern is generated by seven iterations, where the ratio between external and internal slot boundaries obeys the golden ratio, which creates the slot enlargement. Numerical simulations demonstrate multi-band resonances in different microwave frequencies for LP incident  $x$ - and  $y$ -polarization wavefronts. Excellent LP waves splitting are evidenced by high polarization contrast (PC) peaks of 27 dB, making this design promising for future polarization division multiplexing applications.

**Keywords**—Fibonacci Spiral, Metasurfaces, Polarization Control.

## I. INTRODUCTION

Metasurfaces have become a powerful technology for wavefront manipulation across a wide range of spectrum [1], [2]. The ability to control the electromagnetic waves through artificial man-made properties has opened a new path for applications that demand precision, such as wireless communications [3], [4], selective filters [5], [6], sensing [7], [8], imaging [9], [10], among others. In particular, metasurfaces have a great potential to assist wireless communications in reconfigurable intelligent surfaces (RISs) systems to circumvent limitation as coverage, energy efficiency, spectral efficiency and channel reconfigurability [11], [12], [13], [14].

Indeed, this unique properties of metasurfaces can assist communication systems that employ polarization division multiplexing (PDM) technique. PDM relies on the ability to manipulate and maintain orthogonal polarization states, namely, linearly polarized (LP) waves — $x$ -polarization ( $x$ -pol) and  $y$ -polarization ( $y$ -pol)— to transmit multiple independent data streams over the same frequency band and time, effectively doubling the spectral efficiency and system capacity [15], [16]. Metasurfaces can dynamically control and spatially separate orthogonal polarization states, enabling not only real-time polarization control, but also the spatial distribution of independent polarization channels across different regions of space [17], [18]. This capability allows PDM-based systems to cover larger areas or serve multiple users simultaneously with high spectral efficiency and minimal interference. Despite this mature technology is commonly used in satellite broadcasting, radar, and optical fiber communications [15], there is a lack

of studies for LP waves discrimination in terrestrial RF applications.

In recent literature, several studies have investigated the use of metasurfaces to achieve advanced polarization control. For instance, reconfigurable and anisotropic metasurfaces have demonstrated dynamic manipulation of polarization states for beam steering and wavefront shaping [19]. Other works have proposed polarization-dependent transmission or reflection using chiral or asymmetric geometries [20]. Additionally, dual-functional metasurfaces capable of independently modulating LP waves have been reported for polarization beam splitting and selective filtering [21]. These developments highlight the potential of metasurfaces as compact and efficient platforms for polarization control, although challenges remain in achieving wideband operation, high isolation between polarizations, practical integration with communication hardware, and RF applications.

In particular, non-symmetrical metasurfaces can fulfill the requirements of PDM applications, enabling incoming waves to be selectively transmitted or reflected depending on their polarization [22], [23]. Such structures offer a promising alternative for enhancing signal coverage by spatially separating LP waves into distinct coverage regions [18]. However, current approaches often rely on bulky designs, narrowband operation, or limited polarization discrimination, which restrict their applicability in compact, wideband, and high-capacity communication systems.

Leveraging the intrinsic connection between nature and biological systems, this work introduces a novel spiral metasurface inspired by a discrete Fibonacci spiral sequence. The unit-cell consists of two interrelated Fibonacci sequences, geometrically arranged according to the golden ratio to define the slotted element shape. The counter-clockwise sequence progression enables the metasurface to resonantly couple LP waves across distinct spectral regions. As a proof of concept, we demonstrate the concept at microwave frequencies and analyze the spectral response as a function of  $x$ - and  $y$ -pol waves. Operating as a frequency selective surface (FSS), the metasurface exhibits multi-band bandpass filtering within the range of  $1 \text{ GHz} \leq f \leq 14 \text{ GHz}$ . Notably, the frequency selectivity differs for incident  $x$ - and  $y$ -pol waves, resulting in high levels of polarization-dependent separation in the transmitted and reflected signals.

## II. METHODOLOGY

A schematic representation of the proposed spiral-like metasurface is shown in Fig. 1(a). The unit-cell is comprised by a slotted Fibonacci shape, where a discrete sequence increases

William O. F. Carvalho, National Institute of Telecommunications (Inatel), 37536-001, Santa Rita do Sapucaí, Brazil, e-mail: william.orivaldo@inatel.br. This work has been funded by the following research projects: Brasil 6G Project with support from RNP/MCTI (Grant 01245.010604/2020-14), xGMobile Project code XGM-AFCCT-2024-7-9-1 with resources from EMBRAPII/MCTI (Grant 052/2023 PPI IoT/Manufatura 4.0 and FAPEMIG Grant PPE-00124-23)

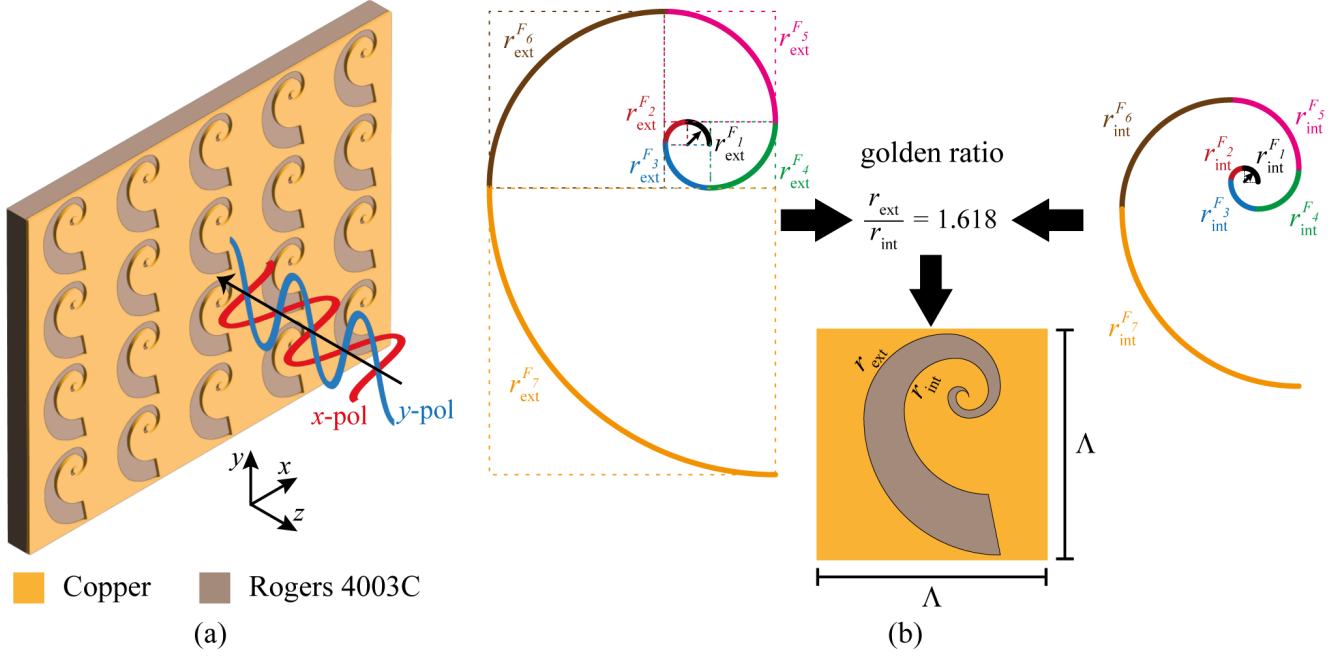


Fig. 1: (a) Schematic of slotted Fibonacci spiral metasurface under incidence of LP microwaves. (b) The unit-cell is designed according to the discrete Fibonacci spiral iterations for external (left) and internal (right) boundaries. This latter is reduced by the golden ratio to outline the slot pattern, shaping the unit-cell seen in the inset.

the slot in counter-clockwise. The periodicity was defined as  $\Lambda$  to meet the subwavelength unit-cells requirements in the analyzed range. As seen in Fig. 1(b), the Fibonacci spiral is a geometric construct derived from the Fibonacci sequence, an integer series defined recursively by  $F_n = F_{n-1} + F_{n-2}$ , with initial terms  $F_1 = 1$  and  $F_2 = 1$ . This spiral is formed by placing squares with side lengths corresponding to successive Fibonacci numbers in a tiling configuration, each oriented at a  $90^\circ$  increment relative to the previous, and inscribing quarter-circle arcs within each square. In this way, the slot induces localized resonances across the entire unit-cell, enabling the coupling of modes in different spectral regions according to  $x$ -pol or  $y$ -pol.

The proposed design incorporates two distinct Fibonacci spirals: one delineating the external boundary of the slot and the other defining its internal border. On the left side of Fig. 1(b), the first quarter-circle of the external boundary is defined with a radius denoted as  $r_{ext}$ , corresponding to the first term of the Fibonacci sequence, i.e.,  $F_1 = r_{ext}$ . Consequently, only two geometric parameters —  $r_{ext}$  and  $\Lambda$  — are required to construct the Fibonacci spiral pattern. The sequence proceeds as follows: the second term is  $F_2 = F_1 = r_{ext}$ , the third is  $F_3 = F_2 + F_1 = 2r_{ext}$ , the fourth is  $F_4 = F_3 + F_2 = 3r_{ext}$ , and so on, up to the seventh iteration, given by  $F_7 = F_6 + F_5 = 13r_{ext}$ . Similarly, on the right side of Fig. 1(b), a Fibonacci spiral with seven iterations is constructed using proportionally reduced quarter-circle arcs, with the first term defined as  $F_1 = r_{int}$ . Both spirals originate from the same coordinates within the unit-cell. Notably, the internal spiral governs the gradual widening of the slot throughout the iterations, as a consequence of the condition  $r_{int} < r_{ext}$  [see the combined spiral structure at the bottom of Fig. 1(b)]. Furthermore, the ratio between  $r_{ext}$

and  $r_{int}$  is selected to follow the natural convergence of the golden ratio, such that  $r_{ext}/r_{int} = 1.618$ . A prototype can be readily fabricated from the resulting pattern, which is fully compatible with standard manufacturing techniques, including conventional computer numerical control (CNC) milling and chemical etching using ferric chloride solution.

Full-wave electromagnetic simulations were carried out using COMSOL Multiphysics®, considering a single metasurface unit-cell element. Floquet periodic boundary conditions were applied along the  $x$ - and  $y$ -directions, while perfectly matched layers (PMLs) were assigned to the  $z$ -boundaries. The metallic layer was modeled as copper with a thickness of  $35 \mu\text{m}$  and electrical conductivity of  $\sigma_{Cu} = 58 \times 10^6 \text{ S/m}$ , deposited on a Rogers® RO4003C substrate of thickness  $t_s = 1.5\text{mm}$ , relative permittivity  $\epsilon_s = 3.55$ , and loss tangent  $\tan \delta = 0.0021$ . The metasurface reflection coefficient,  $S_{11}$ , expressed in decibels (dB), was evaluated over the frequency range  $1 \text{ GHz} \leq f \leq 14 \text{ GHz}$  under normal incidence along the  $-z$  direction, for both linearly  $x$ - and  $y$ -pol waves. To ensure multi-band resonant behavior without diffraction effects at microwave frequencies, the unit-cell period was set to  $\Lambda = 22 \text{ mm}$ . The initial quarter-circle radius were defined as  $r_{ext}^{F_1} = 1 \text{ mm}$  and  $r_{int}^{F_1} = 0.618 \text{ mm}$ , ensuring that subsequent iterations followed the Fibonacci sequence scaled by the golden ratio.

### III. RESULTS AND DISCUSSION

Fig. 2(a) illustrates the reflection coefficients for both  $x$ -pol (in red) and  $y$ -pol (in blue) incident wavefronts using  $r_{ext} = 1 \text{ mm}$ . The slotted unit-cells are responsible for the excitation of multiple resonances across the analyzed frequency range. Notably, the spectral responses differ significantly between  $x$ - and  $y$ -pol incident waves. At lower frequencies

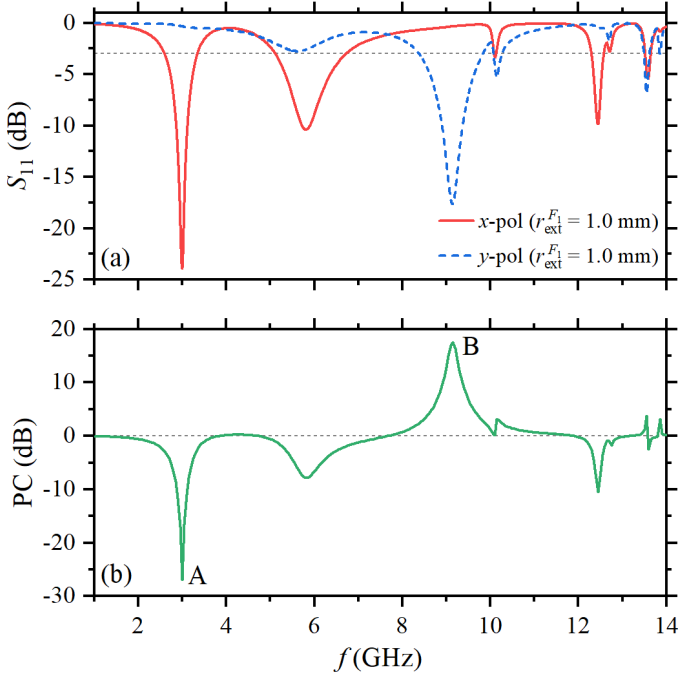


Fig. 2: (a) Reflectances for  $x$ -pol (red) and  $y$ -pol (blue) incident waves and (b) the PC results.

(below  $f = 6$  GHz), the response is predominantly governed by  $x$ -pol resonances, whereas at higher frequencies (above  $f = 9$  GHz), distinct  $y$ -pol resonances emerge. Specifically, the  $x$ -pol exhibits three prominent reflection dips below  $S_{11} < -3$  dB within the analyzed range, with bandwidths of  $BW = 0.75$  GHz,  $BW = 1.60$  GHz, and  $BW = 0.28$  GHz are achieved at their respective center frequencies of  $f = 3$  GHz,  $f = 5.8$  GHz, and  $f = 12.45$  GHz. On the other hand,  $y$ -pol shows only a single notable dip at center frequency  $f = 9.15$  GHz with a bandwidth of  $BW = 1.46$  GHz. At higher frequencies, additional resonance features are anticipated due to the finer geometrical details of the spiral structure. The reflected spectra clearly diverge, indicating distinct mode coupling mechanisms within the slotted metasurface for each polarization. These resonances exhibit exceptional bandpass behavior, suggesting that at specific frequencies, either  $x$ - or  $y$ -pol waves are efficiently transmitted through the metasurface.

The discrepancies observed between the reflected waves for orthogonal polarizations can be used to assess the polarization-selective performance of the metasurface, quantified here by the so-called polarization contrast (PC) parameter. The PC parameter evaluates the difference between  $x$ - and  $y$ -polarizations and is defined as

$$PC_{x,y} \text{ (dB)} = S_{11}^x \text{ (dB)} - S_{11}^y \text{ (dB)}, \quad (1)$$

expressed in dB. The superscripts  $x$  and  $y$  denote the reflection coefficients  $S_{11}$  for  $x$ - and  $y$ -pol incident waves, respectively. In addition to supporting multi-band resonances, the metasurface exhibits pronounced polarization selectivity, as evidenced by high PC values. For instance, at  $f = 3$  GHz and  $f = 9.15$  GHz (labeled as points A and B), the PC reaches  $PC = -26.96$  dB and  $PC = 17.61$  dB, respectively, as shown in Fig. 2(b). These values indicate strong polarization discrimination, where

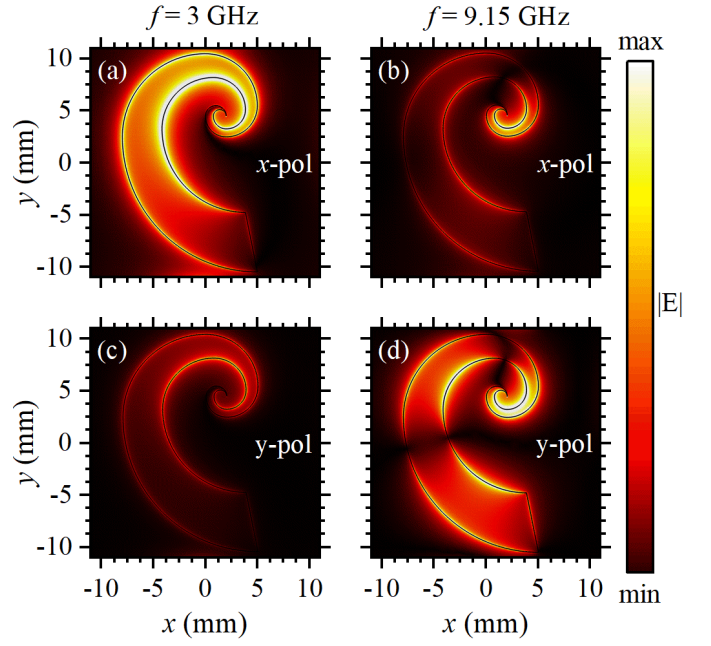


Fig. 3: Normalized electric field profiles for (a)-(b)  $x$ -pol and (c)-(d)  $y$ -pol under incident frequency of  $f = 3$  GHz (point A) and  $f = 9.15$  GHz (point B).

negative PC values corresponds to high transmission (reflection) for  $x$ -pol ( $y$ -pol) and positive PC values corresponds to high transmission (reflection) for  $y$ -pol ( $x$ -pol). Such behavior demonstrates the potential of this metasurface for polarization control of propagating waves, thereby enabling applications in PDM wireless communication systems.

Fig. 3 presents the electric near-field distributions at the resonance frequencies corresponding to points A and B in Fig. 2(b). The first row corresponds to the field profiles under  $x$ -pol excitation, while the second row illustrates the results for  $y$ -pol waves. All field maps are normalized by the same factor to facilitate a direct comparison of the coupling intensities under resonant conditions. In Fig. 3(a), a strong electric field enhancement is observed at  $f = 3$  GHz for the  $x$ -pol, confirming the presence of a resonance. Conversely, Fig. 3(d) shows pronounced field localization at  $f = 9.15$  GHz under  $y$ -pol excitation, indicating a resonance for this polarization. In contrast, the field profiles shown in Figs. 3(b)-(c) exhibit weak field coupling into the slotted structure, suggesting that the incident waves do not excite resonant modes, resulting in high reflection levels.

The polarization-dependent coupling behavior can be attributed to the counter-clockwise orientation of the spiral, which results in a vertical-like slot structure at the final iteration. As a result,  $x$ -pol modes dominate over  $y$ -pol modes, as observed in Fig. 2(a). This dominance is primarily associated with dipoles formed along various regions of the slot boundaries. The coupling of modes is confined to specific segments of the slot, depending on the frequency. For example, at  $f = 3$  GHz, shown in Fig. 3(a), the coupled  $x$ -pol wave is predominantly confined to the internal boundary of the slot near the iterations  $r_{\text{int}}^{F_5}$  and  $r_{\text{int}}^{F_6}$  [see Fig. 1(b) for details].

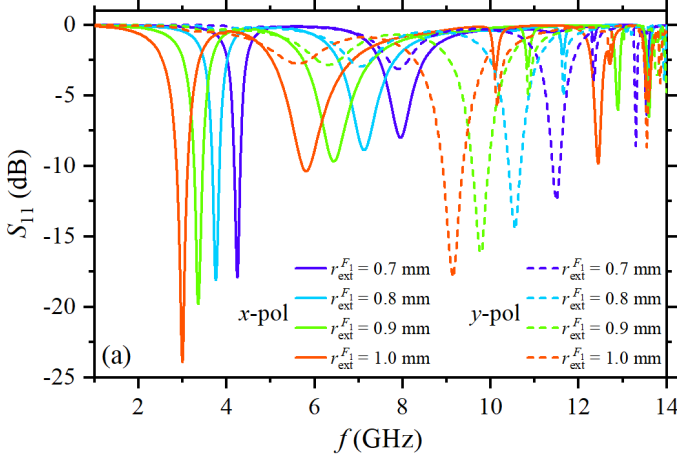


Fig. 4: Reflectances in function of  $r_{\text{ext}}^{F_1}$  for  $x$ -pol (solid) and  $y$ -pol (dashed).

In contrast, at  $f = 9.15$  GHz [Fig. 3(b)], the  $x$ -pol wave is mainly localized around the iterations  $r_{\text{int}}^{F_3}$  and  $r_{\text{int}}^{F_4}$ , though with a lower field intensity. Similarly, for  $y$ -pol, at  $f = 3$  GHz [Fig. 3(c)], the coupling levels are low in the same  $x$ -pol region. However, at  $f = 9.15$  GHz [Fig. 3(d)], a stronger coupled mode is observed for the  $y$ -pol wave, with three main localized electric field regions appearing at the boundaries corresponding to  $r_{\text{int}}^{F_3}$ ,  $r_{\text{int}}^{F_4}$ ,  $r_{\text{int}}^{F_6}$ , and  $r_{\text{int}}^{F_7}$ . This suggests that as the number of iterations increases (starting with  $r_{\text{ext}}^{F_1} = 1$  mm and  $r_{\text{int}}^{F_1} = 0.618$  mm), lower frequencies tend to couple more efficiently at the spiral slots.

To investigate the impact of the initial term  $r_{\text{ext}}^{F_1}$  on the frequency response of LP waves, we analyze four different slotted unit-cells, as shown in Fig. 4, as a function of  $r_{\text{ext}}^{F_1}$ , namely,  $r_{\text{ext}}^{F_1} = 1.0$  mm,  $r_{\text{ext}}^{F_1} = 0.9$  mm,  $r_{\text{ext}}^{F_1} = 0.8$  mm, and  $r_{\text{ext}}^{F_1} = 0.7$  mm, while keeping the unit-cell period  $\Lambda = 22$  mm constant across all simulations. It is important to note

TABLE I:  
RADIUS OF THE SEVEN FIBONACCI ITERATIONS.

	$r_{\text{ext}}^{F_1} = 1.0\text{mm}$		$r_{\text{ext}}^{F_1} = 0.9\text{mm}$		$r_{\text{ext}}^{F_1} = 0.8\text{mm}$		$r_{\text{ext}}^{F_1} = 0.7\text{mm}$	
	$r_{\text{ext}}$	$r_{\text{int}}$	$r_{\text{ext}}$	$r_{\text{int}}$	$r_{\text{ext}}$	$r_{\text{int}}$	$r_{\text{ext}}$	$r_{\text{int}}$
$F_1$	1.0	0.618	0.9	0.556	0.8	0.494	0.7	0.432
$F_2$	1.0	0.618	0.9	0.556	0.8	0.494	0.7	0.432
$F_3$	2.0	1.236	1.8	1.112	1.6	0.988	1.4	0.865
$F_4$	3.0	1.854	2.7	1.669	2.4	1.483	2.1	1.297
$F_5$	5.0	3.091	4.5	2.781	4.0	2.472	3.5	2.163
$F_6$	8.0	4.944	7.2	4.449	6.4	3.955	5.6	3.461
$F_7$	13	8.035	11.7	7.231	10.4	6.427	9.1	5.624

that  $r_{\text{int}}$  is related to  $r_{\text{ext}}$  by the golden ratio. For clarity, Table I provides a summary of all the  $r_{\text{ext}}$  and  $r_{\text{int}}$  dimensions derived from the values of  $r_{\text{ext}}^{F_1}$ . As observed, reflection dips appear at different frequency points for  $x$ -pol (solid curves) and  $y$ -pol (dashed curves). Given that the unit-cell period  $\Lambda$  is fixed, a slight blue-shift is noted as  $r_{\text{ext}}$  decreases for both polarizations, as expected. This result underscores the need for precise fabrication control of the Fibonacci spiral metasurfaces, which can be easily achieved using CNC milling. This method enables accurate copper removal and automated cutting based on pre-programmed designs with high resolution [24].

To gain a deeper understanding of the PC performance, we illustrate in Fig. 5 the response of the proposal under oblique wave incidence. Specifically, Fig. 5(a) shows the angle  $\theta$  in the  $xz$ -plane for  $x$ -pol (TM waves) and  $y$ -pol (TE waves) incidence, with the corresponding results presented in Figs. 5(c) and 5(d), respectively. Similarly, Fig. 5(b) depicts the incident angle  $\phi$  in the  $yz$ -plane for  $x$ -pol (TE waves) and  $y$ -pol (TM waves), with the corresponding results shown in Figs. 5(e) and 5(f). In Fig. 5(c), the spectral reflection responses are shown as a function of the incident angle  $\theta$ , with solid curves representing

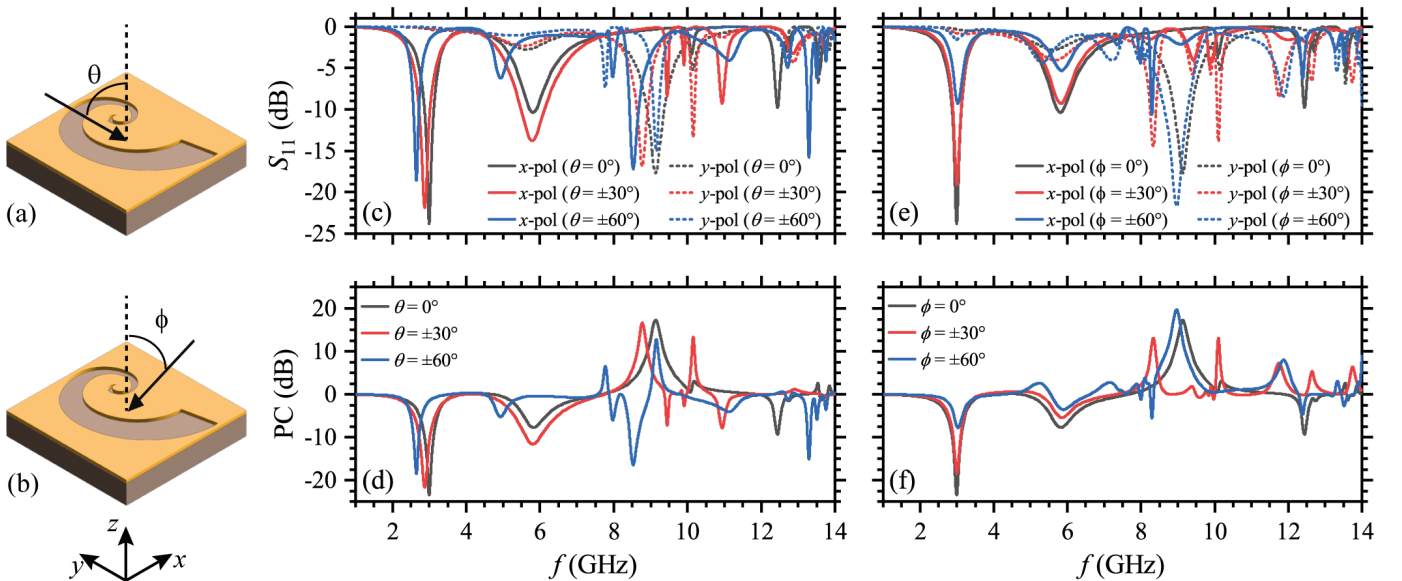


Fig. 5: Performance variation in function of oblique angles (a)  $\theta$  or (b)  $\phi$ . (c) Reflectances and (d) PC for sweeping  $\theta$ . (e) Reflectances and (f) PC for sweeping  $\phi$ .



$x$ -pol and dotted curves representing  $y$ -pol. Notably, small reflectance discrepancies are observed at  $f = 3$  GHz for  $x$ -pol and at  $f = 9.15$  GHz for  $y$ -pol, while more significant changes occur at  $f = 6$  GHz for  $x$ -pol. A similar trend is observed in Fig. 5(e), which shows the response as a function of the incident angle  $\phi$ .

The observed variations in reflectance due to changes in the incident angles are reflected in the PC levels shown in the second row of Fig. 5. For the  $\theta$ -sweeping results in Fig. 5(d), the PC remains similar to that observed under normal incidence at  $f = 3$  GHz, but shows significant differences at  $f = 9.15$  GHz. This discrepancy is primarily attributed to the emergence of new resonant modes under oblique wave incidence, which respect the phase matching of surface waves. Specifically, for  $\theta = \pm 60^\circ$ , the blue-solid curve exhibits greater PC fluctuations, which can be linked to a new resonant coupled mode for  $x$ -pol around  $f = 8.5$  GHz, as indicated by the blue-solid line in Fig. 5(c). In contrast, no significant variation in PC levels is observed in Fig. 5(f). Despite the reflectance variations observed in Fig. 5(e) for the  $\phi$ -sweeping, the PC remains stable for angles  $\phi \leq \pm 60^\circ$ , with only minimal additional coupled modes emerging at  $\phi = \pm 30^\circ$  (in red-solid curve).

#### IV. CONCLUSIONS

In conclusion, we have demonstrated a microwave slotted metasurface capable of controlling LP waves with multi-band functionalities. This was achieved using sub-wavelength unit-cells comprised of slots arranged in a Fibonacci spiral design, fabricated on a copper laminate over a substrate. The design follows a discrete Fibonacci sequence up to the seventh iteration, generating quarter-circle arcs for the external ( $r_{\text{ext}}$ ) and internal ( $r_{\text{int}}$ ) boundaries, in accordance with the golden ratio. The metasurface effectively transmitted and reflected specific frequencies based on  $x$ -pol and  $y$ -pol wavefronts. Polarization control was demonstrated through the evaluation of PC, where prominent peaks indicated significant separation between LP waves, managing the transmission (reflection) of  $x$ -pol ( $y$ -pol) waves and vice versa. Further analysis, varying the initial radius  $r_{\text{ext}}^{F_1}$  and  $r_{\text{int}}^{F_1}$ , showed a linear displacement of resonances. Additionally, the reliability of the results was confirmed by the PC behavior under oblique incidence, where high PC levels exhibited minimal fluctuations. This behavior opens promising opportunities for advanced polarization control in communication systems, sensing, and imaging. The multi-band features of the Fibonacci spiral-inspired design also provide a scalable framework for the development of future metasurfaces across different frequency regimes, paving the way for novel polarization control applications in PDM wireless communications.

#### REFERENCES

- [1] A. Li, S. Singh, and D. Sievenpiper, "Metasurfaces and their applications," *Nanophotonics*, vol. 7, no. 6, pp. 989–1011, 2018.
- [2] V. G. Ataloglou, S. Taravati, and G. V. Eleftheriades, "Metasurfaces: physics and applications in wireless communications," *Natl. Sci. Rev.*, vol. 10, no. 8, p. nwad164, 2023.
- [3] H. L. Wang, H. F. Ma, and T. J. Cui, "A polarization-modulated information metasurface for encryption wireless communications," *Adv. Sci.*, vol. 9, no. 34, p. 2204333, 2022.
- [4] Z. X. Wang, J. W. Wu, H. Xu, J. Y. Dai, S. Liu, Q. Cheng, and T. J. Cui, "A dual-polarization programmable metasurface for green and secure wireless communication," *Adv. Sci.*, vol. 11, no. 32, p. 2403624, 2024.
- [5] Q. Lv, X. Qin, M. Hu, P. Li, Y. Zhang, and Y. Li, "Metatronics-inspired high-selectivity metasurface filter," *Nanophotonics*, vol. 13, no. 16, pp. 2995–3003, 2024.
- [6] N. Goshen and Y. Mazar, "Single-layer, all-metallic metasurface filter with nearly  $90^\circ$  angularly stable resonance," *IEEE Trans. Antennas Propag.*, 2024.
- [7] J. Zhao, L. Zhang, and H. Liang, "Advances in metasurface-based terahertz sensing," *Adv. Phys. Res.*, vol. 3, no. 12, p. 2400077, 2024.
- [8] W. O. F. Carvalho, O. N. Oliveira, and J. R. Mejía-Salazar, "Magnetochiroptical nanocavities in hyperbolic metamaterials enable sensing down to the few-molecule level," *J. Chem. Phys.*, vol. 160, no. 7, 2024.
- [9] Y. Luo, X. Li, R. Zhang, Y. Guo, M. Pu, Y. Fan, Q. Zhang, Q. He, J. Che, Z. Zhao *et al.*, "Monocular metasurface for structured light generation and 3D imaging with a large field-of-view," *ACS Appl. Mater. Interfaces*, vol. 16, no. 30, pp. 39 906–39 916, 2024.
- [10] M. Zhao, S. Zhu, D. Li, T. Fromenteze, M. Khalily, X. Chen, V. Fusco, and O. Yurduseven, "Frequency-diverse bunching metasurface antenna for microwave computational imaging," *IEEE Trans. Antennas and Propag.*, 2024.
- [11] H. Xue, Z. Lu, X. Ma, Z. Wang, L. Zhu, S. Yue, J. Han, H. Liu, and L. Li, "A reconfigurable metasurface enhancing signal coverage for wireless communication using reduced numbers of p-i-n diodes," *IEEE Trans. Microw. Theory Tech.*, vol. 72, no. 3, pp. 1964–1978, 2023.
- [12] M. Ahmed, S. Raza, A. A. Soofi, F. Khan, W. U. Khan, S. Z. U. Abideen, F. Xu, and Z. Han, "Active reconfigurable intelligent surfaces: Expanding the frontiers of wireless communication—a survey," *IEEE Commun. Surv. Tutor.*, 2024.
- [13] F. Bilotti, M. Barbuto, Z. Hamzavi-Zarghani, M. Karamirad, M. Longhi, A. Monti, D. Ramaccia, L. Stefanini, A. Toscano, and S. Vellucci, "Reconfigurable intelligent surfaces as the key-enabling technology for smart electromagnetic environments," *Adv. Phys.: X*, vol. 9, no. 1, p. 2299543, 2024.
- [14] J. H. Park, S. H. Kim, M. M. Amri, N. M. Tran, D. I. Kim, and K. W. Choi, "Uplink MIMO communications with ris-integrated base station: Modeling and experiments," *IEEE Internet Things J.*, Early Access, 2025.
- [15] C. Guo, F. Liu, S. Chen, C. Feng, and Z. Zeng, "Advances on exploiting polarization in wireless communications: Channels, technologies, and applications," *IEEE Commun. Surv. Tutor.*, vol. 19, no. 1, pp. 125–166, 2016.
- [16] Z. Yuan, Y. Wang, H. Fan, X. Liu, M. Cheng, Q. Yang, M. Tang, D. Liu, and L. Deng, "Multichannel parallel mode order converter for on-chip reconfigurable PDM-MDM transmission," *Laser Photonics Rev.*, vol. 19, no. 9, p. 2401689, 2025.
- [17] M. Liu, W. Zhu, P. Huo, L. Feng, M. Song, C. Zhang, L. Chen, H. J. Lezec, Y. Lu, A. Agrawal *et al.*, "Multifunctional metasurfaces enabled by simultaneous and independent control of phase and amplitude for orthogonal polarization states," *Light: Sci. Appl.*, vol. 10, no. 1, p. 107, 2021.
- [18] X. Tan, R. Yang, S.-L. Chen, K. F. Chan, B. J. Chen, Z.-Q. Cui, P.-Y. Qin, Y. J. Guo, and C. H. Chan, "Highly integrated full-space coding metasurface for LP and CP waves manipulation spanning millimeter-wave and sub-THz bands," *J. Lightw. Technol.*, vol. 43, no. 1, pp. 288–298, 2025.
- [19] H. Yang, X. Cao, F. Yang, J. Gao, S. Xu, M. Li, X. Chen, Y. Zhao, Y. Zheng, and S. Li, "A programmable metasurface with dynamic polarization, scattering and focusing control," *Sci. Rep.*, vol. 6, no. 1, p. 35692, 2016.
- [20] B. Yang, M. Ouyang, H. Ren, J. Wu, Y. Zhang, and Y. Fu, "Polarization-dependent absorption and transmission metasurfaces for linearly and circularly polarized light in terahertz band," in *Photonics*, vol. 10, no. 2. MDPI, 2023, p. 100.
- [21] Z. Shen and D. Huang, "A review on metasurface beam splitters," *Nanomanufacturing*, vol. 2, no. 4, pp. 194–228, 2022.
- [22] W. Liu, X. Jiang, Q. Xu, F. Huang, Q. Yang, Y. Lu, Y. Gu, J. Gu, J. Han, and W. Zhang, "All-dielectric terahertz metasurfaces for multi-dimensional multiplexing and demultiplexing," *Laser Photonics Rev.*, vol. 18, no. 8, p. 2301061, 2024.
- [23] S. Baek, H. Son, H. Park, H. Park, J. Lee, S. Jeong, J.-E. Shim, J. Park, and T.-T. Kim, "Graphene-based metasurface: dynamic optical control in ultrathin flat optics," *Nanophotonics*, no. 0, 2025.
- [24] W. O. F. Carvalho, J. J. H. Sarria, L. L. Mendes, and J. R. Mejía-Salazar, "Cartesian multipole expansion for millimeter-wave metasurfaces design," *J. Appl. Phys.*, vol. 137, no. 9, 2025.